Research Article Vol. 4, No. 10 / October 2017 / Optica 1180

Fiber interferometer for hybrid optical and optoacoustic intravital microscopy

Rami Shnaiderman,[1,2,†] Georg Wissmeyer,[1,2,†] Markus Seeger,[1,2] Dominik Soliman,[1,2] Hector Estrada,[1] Daniel Razansky,[1,2] Amir Rosenthal,[1,2,3] and Vasilis Ntziachristos[1,2,*]

[1]Institute for Biological and Medical Imaging, Helmholtz Zentrum München, Neuherberg 85764, Germany
[2]Chair for Biological Imaging, Technische Universität München, München 81675, Germany
[3]Andrew and Erna Viterbi Faculty of Electrical Engineering, Technion — Israel Institute of Technology, Haifa 32000, Israel
*Corresponding author: v.ntziachristos@tum.de

Received 30 November 2016; revised 5 July 2017; accepted 18 July 2017 (Doc. ID 281853); published 29 September 2017

The addition of optoacoustic sensing to optical microscopy may supplement fluorescence contrast with label-free measurements of optical absorption, enhancing biological observation. However, the physical dimensions of many optoacoustic systems have restricted the implementation of hybrid optical and optoacoustic (O2A) microscopy to imaging thin samples in transmission mode or to *ex-vivo* investigations. Here we describe a miniaturized optoacoustic sensor, based on a π-phase-shifted fiber Bragg grating embedded in an acoustic cavity, which is virtually invisible to the optical path and can be seamlessly integrated into any conventional optical microscope. The new sensor enables, for the first time to our knowledge, entirely optical O2A intravital microscopy in epi-illumination mode, demonstrated by label-free optoacoustic and second-harmonic generation images of a mouse abdomen and ear. Our technique greatly simplifies the integration of acoustic detection in standard microscopes and could therefore make optoacoustic microscopy more accessible to the biomedical community.

OCIS codes: (170.3880) Medical and biological imaging; (180.0180) Microscopy; (110.5125) Photoacoustics; (060.3735) Fiber Bragg gratings; (060.2370) Fiber optics sensors.

https://doi.org/10.1364/OPTICA.4.001180

1. INTRODUCTION

Fluorescent proteins (FPs) have broadened the use of optical microscopy to intravital measurements of biological function [1,2]. Modern trends in biological imaging are moving toward the concurrent assessment of an ever-increasing number of sub-cellular parameters. Spectral imaging of FPs that emit at different wavelengths can enable parallel imaging of different biological processes [3]. However, co-expression of multiple FPs may alter cell function or have toxic effects. The use of externally administered fluorescence agents targeting cellular moieties can potentially increase the number of independent observations [4], but their use is limited by agent bio-distribution and the specificity of the agent for the biomarker targeted.

To allow visualization of structure and function without the need for reporter genes or exogenous agents, several types of label-free optical microscopy methods have been proposed. Second- and third-harmonic generation [5] or Raman imaging [6] have been employed to visualize specific tissue or cellular structures and molecular species without labeling techniques. In addition, we have recently proposed the use of hybrid optical and optoacoustic (O2A) microscopy, merging conventional optical readings with label-free optoacoustic (absorption) contrast [7]. O2A has been shown to concurrently resolve fluorescence, non-linear absorption, and optical absorption in biological specimens [8–11]. A limitation of O2A microscopy is that the sample must be in close proximity to both a microscope objective (to collect light from the specimen) and an ultrasound transducer (to detect acoustic signal from the specimen). However, optical objectives and highly sensitive ultrasound transducers come at sizes that are typically much larger than the sample or volume imaged. As a result, they cannot be co-localized. Consequently, many O2A implementations are performed in transmission mode [12], i.e., by placing the specimen between the objective and a focused ultrasound transducer.

Epi-illumination (reflection) O2A imaging could be achieved using small ultrasound detection elements placed in close proximity to the objective [13]. However, miniaturization of ultrasound detectors based on ceramic compounds is problematic. The sensitivity of piezoelectric elements is proportional to the size of the active surface; therefore, miniaturization leads to a quadratic decline in detection sensitivity. For example, miniaturized piezoelectric elements used for intravascular ultrasound detection (IVUS, Boston Scientific) have a sensing surface with a diameter of 1.2 mm, noise-equivalent pressure (NEP) of 1.8 kPa, and bandwidth of 16 MHz [14]. In contrast, optoacoustic microscopy requires ultrasound detectors with NEP < 100 Pa [15]. Moreover, the ultrasound frequency detected depends on the thickness of the piezoelectric element; as a result, miniaturization

may also constrain the frequency bandwidth that can be detected. While ultrasound losses can be minimized by placing miniaturized piezoelectric detectors in front of the microscope objective [13,16], this practice blocks direct tissue illumination and requires costly, specialized objectives with high numerical aperture (NA). In addition, this approach leads to blurring when imaging thick samples because tight (high-NA) focusing generates conical axial illumination, making different objects, such as 3D capillary networks, appear out of focus. Optoacoustic microscopy with large piezoelectric transducers has also been considered using acoustically reflecting but optically transparent prisms [17]. This approach results in detectors of large form factors and typically imposes longer sound propagation paths, compared to the use of miniaturized elements, that attenuate high frequencies (e.g., >25 Mhz) [18]. Such a detector has not yet been demonstrated to allow O2A imaging. A recent approach, based on converting nonradiative optical de-excitation into acoustic pressure with an optoacoustic cell, showed promising results for high-resolution epi-illumination OAM [19]. However, this approach relies on strict thermal isolation of the sample and might impede an easy implementation into existing microscopy setups as well as the imaging of larger specimens, such as mouse models.

All-optical ultrasound detectors offer a promising alternative to piezoelectric detectors for O2A implementations in reflection mode. Optical sensors that are based on the detection of acoustically induced refractive index changes as well as optical resonators have been shown recently [20–22]. In particular, resonator-based optical interferometry was demonstrated as a promising approach for O2A, as it allows the design of optoacoustic detection elements at ultra-small dimensions and miniaturization without loss of bandwidth and sensitivity. Likewise, the small form factor permits an implementation into existing microscopy setups without modifications to its optics. Micro-ring resonators have been proposed for optoacoustic microscopy in transmission and epi-illumination modes [23,24]. However, the bandwidth of ultrasound frequencies that can be detected with micro-ring resonators depends strongly on acceptance angle: high-bandwidth detection can only be achieved over a narrow 7° detection angle. Such low detection angle yielded small fields of view (~100 μm × 100 μm) when coupled to high-NA microscope objectives, which limited applications to imaging small samples such as blood cells smeared on a cover slip [25]. Optoacoustic microscopy in transmission mode has been also demonstrated based on π-phase-shifted fiber Bragg grating (π-FBG) interferometry and achieved NEP of 100 Pa and fractional bandwidths of 100% and 21% around the respective central frequencies of 20 and 70 MHz [26]. To achieve this performance, the π-FBG detector was interrogated by coherence-restored pulsed interferometry (CRPI), which boosts sensitivity by 40-fold over interrogation with low-coherence sources but is prohibitively expensive for widespread use [27]. Nevertheless, neither ring resonators nor π-FBG-based detectors have enabled intravital O2A imaging in epi-illumination mode for imaging thick samples. In analogy to optical intravital microscopy [28,29], O2A microscopy of thick tissues is critical for deciphering *in vivo* physiology and biology in large specimens such as animals or humans, especially when using a label-free method that can be applied in a safe manner, without high regulatory burden.

In this work, we aim to comprehensively address prior limitations of O2A imaging and deliver a potent ubiquitous sensor that can be employed with any optical microscope objective to allow, for the first time to our knowledge, entirely optical intravital O2A microscopy in epi-illumination mode. To achieve this goal, we develop a new sensor based on π-FBG interferometry. A key hypothesis in the study was that we could deliver O2A intravital microscopy in epi-illumination mode by using an appropriately designed acoustic cavity to improve the performance of π-FBG-based detection over previous reports, while drastically reducing the cost. The strategy behind this ambitious goal and the specifications and intravital performance of the new O2A sensor in thin and thick tissue are explained in the following.

2. MINIATURIZED O2A SENSOR WITH ACOUSTIC SIGNAL AMPLIFICATION

The sensor comprises a metal sleeve, an ellipsoidal acoustic cavity, and a fiber-based π-FBG ultrasound detector [Figs. 1(a)–1(c)]. The π-FBG detector has a diameter of 125 μm and an active detection area of 125 μm × 300 μm, and is inserted into the acoustic cavity through two concentric openings on the cavity side [Fig. 1(b)]. The metal sleeve acts as an adaptor to fit the acoustic

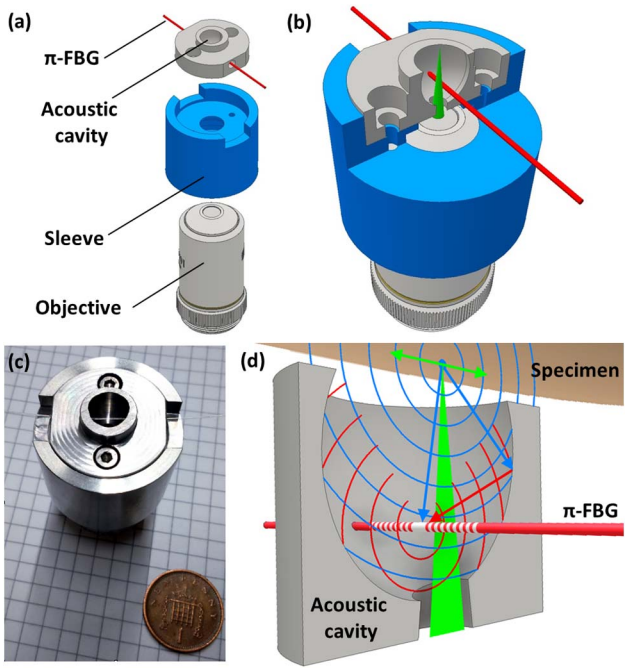

Fig. 1. Design and operating principle of the π-FBG-based sensor. (a) Perspective view of components prior to assembly, showing the acoustic cavity, metal sleeve (adapter), and microscope objective. The red line indicates the position of the π-FBG fiber through the acoustic cavity. (b) Schematic of the assembled sensor head with cross-sectional view of the acoustic cavity. (c) Photograph of the acoustic cavity mounted on the sleeve, next to a UK penny for size comparison. The π-FBG detector traverses the cavity. (d) Cross-section of the acoustic cavity illustrating the operating principle of the π-FBG sensor. The laser beams for second-harmonic generation and optoacoustic excitation (green cone) enter the reflector from the opening at the bottom and focus inside the specimen. The green arrows indicate the region of interest scanned by the excitation beams. Upon absorption, optical signals are collected by the microscope objective below the cavity (not shown); optoacoustic signals enter the acoustic cavity (blue circles), where they are reflected and focused (red circles) onto the active detection area of the π-FBG detector located at the inner acoustic focus of the ellipsoidal cavity.

cavity to the microscope objective. To enable intravital epi-illumination performance, the sensor was designed with five unique and critical features:

First, the acoustic cavity has an ellipsoidal shape, which allows bifocal acoustic focus and thereby virtually eliminates interference between the microscope's optical path and the π-FBG detector. Tilting the ellipsoid on its minor axis by 12° in relation to the plane of the microscope objective places the first acoustic focus 400 μm from the rim of the cavity. This distance was chosen for an imaging depth adequate for studying mouse dermis, and it matches the depths imaged by multi-photon microcopy. The second acoustic focus is located 5 mm away from the first focus, inside the cavity along its major axis. The first acoustic focus is centered on the optical focus while the π-FBG detector is placed to coincide with the second acoustic focus inside the cavity [Fig. 1(d)]. This configuration implements an *acoustic path* that differs from the *optical path* between the microscope objective and the sample.

Second, measuring 9.6 mm along the major axis and 8.2 mm along the minor axis, the cavity collects and focuses ultrasound waves onto the π-FBG detector, effectively amplifying the detected signal by 5 times. These dimensions were chosen to maximize the solid angle of the sensor while not exceeding the working distance of the microscope objective (see methods). The solid angle is a measure for the amount of collected acoustic signals from the first focal point and therefore a measure for the signal amplification.

Third, signal amplification has allowed the use of continuous wave (CW) laser interrogation of the π-FBG (see Methods), enabling cost reduction by a factor of 10 and improving robustness and form factor over previously reported approaches using CRPI [14].

Fourth, the acoustic cavity has a relatively large aperture with a diameter of 7.3 mm, expanding the field of view (FOV) to at least 0.63 mm × 0.63 mm. This large FOV enables fast scanning speeds when combined with galvanometric mirrors.

Fifth, the sensor design can be adjusted to a multitude of optical microscopes by adapting the acoustic cavity and the metal sleeve, depending on the working distance and the NA of the objective.

The acoustic cavity is filled with centrifuged ultrasound gel and sealed with polyethylene foil of 10 μm thickness. A drop of water or ultrasound gel couples the sensor to the specimen without the need for a water tank. Upon excitation, optical signals are collected by the microscope objective by conventional epi-illumination microscopy. Optoacoustic signals, in contrast, enter the acoustic cavity and travel to the π-FBG detector (direct signal) or are reflected within the cavity (indirect signal) and focused onto the detector [Fig. 1(d)]. Indirect contributions arrive approximately 3 μs after the direct signal.

A phantom of black polystyrene sutures (19 μm diameter) arranged in a cross shape was raster-scanned with galvanometric mirrors using a focused beam, and the direct and indirect optoacoustic signals were observed (Fig. 2). The direct response [Fig. 2(a)(i)] exhibited markedly smaller intensity compared to the cavity-amplified indirect response [Fig. 2(a)(ii)]. Differences in frequency bandwidth for direct and indirect contributions [Fig. 2(b)] can be explained if the frequency response of the cavity and ultrasound attenuation inside the cavity are considered (see Methods).

The axial resolution of the system can be approximated from the bandwidth [7], and was estimated to be 37 μm. Images of the sutures were acquired over a FOV of 630 μm × 630 μm using the direct signal [Fig. 2(c)] or the indirect signal [Fig. 2(d)], and were plotted as maximum intensity projections (MIPs). Signal to noise ratio (SNR) analysis exhibited a greater than five-fold improvement when observing images acquired based on the indirect signal, resulting in a clearly observed contrast improvement in Fig. 2(d) compared to Fig. 2(c). In particular, the sutures in Fig. 2(d) are visible over the entire FOV, suggesting a detection angle of at least 76.5°. This enables imaging of large FOVs without the need to move the detector. Images of a block of polished silicon-on-isolator (SOI) wafer [Fig. 2(e)] determined a lateral resolution of 3.7 μm [Figs. 2(f) and 2(g)] for the optical objective employed. This is in reasonable agreement with the theoretical focus diameter of 2.6 μm, and the deviation can be attributed to aberrations and dispersion in the acoustic cavity.

To examine whether our sensor would allow intravital microscopy of thin tissues in epi-illumination mode, we imaged a mouse ear *in vivo*. Stitching together scans of the mouse pinna allowed optoacoustic imaging over an area of 2 mm × 2 mm [Fig. 3(a)], revealing vasculature spanning a wide range of diameters in good detail. Two regions of interest, with an area of 180 μm × 180 μm from the two locations indicated by (i) and (ii) on Fig. 3(a), are

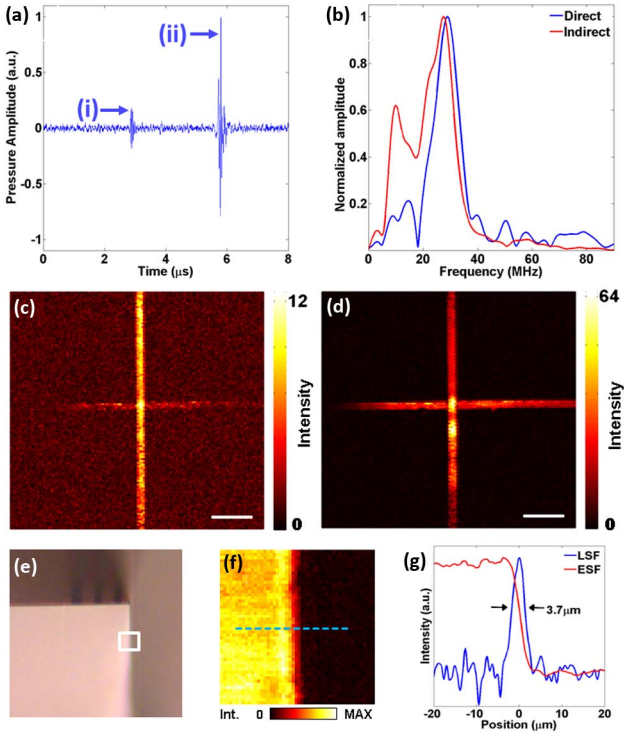

Fig. 2. Characterization of the O2A sensor using (a)–(d) polystyrene sutures and (e)–(g) SOI block. (a) Optoacoustic signals from a polystyrene suture in the time domain, showing a recording of the direct signal (i) and the indirect signal reflected and amplified by the acoustic cavity (ii). (b) Corresponding frequency response of the sensor for direct signal (blue) and indirect signal (red). (c) Maximum intensity projection of the signal recorded directly by the π-FBG. Scale bar, 100 μm. (d) Maximum intensity projection of the cavity-reflected signal. Scale bar, 100 μm. (e) Bright-field optical microscopy image of the polished front of the SOI block, where the indicated area (32 μm × 32 μm) was imaged using optoacoustic microscopy. (f) Maximum intensity projection of the indicated area. (g) Edge spread function and line spread function of the intensity along the blue dashed line in (f).

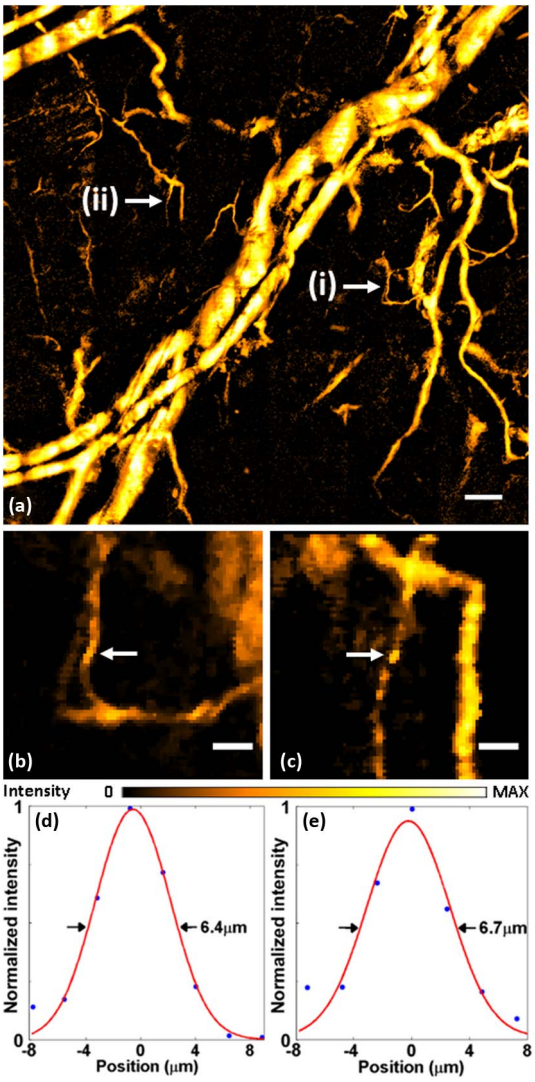

Fig. 3. Optoacoustic microscopy images of a mouse ear *in vivo*. (a) Stitched image of a 2 mm × 2 mm field of view showing complex vasculature with vessels ranging in diameter from 6 to 130 μm. Scale bar, 150 μm. The areas labeled as (i) and (ii) are shown at higher magnification in (b) and (c), respectively (field of view, 180 μm × 180 μm). Scale bars, 30 μm. (d, e) Gaussian fitting of the intensity in the cross-section of vessels indicated with arrows in (b) and (c), respectively.

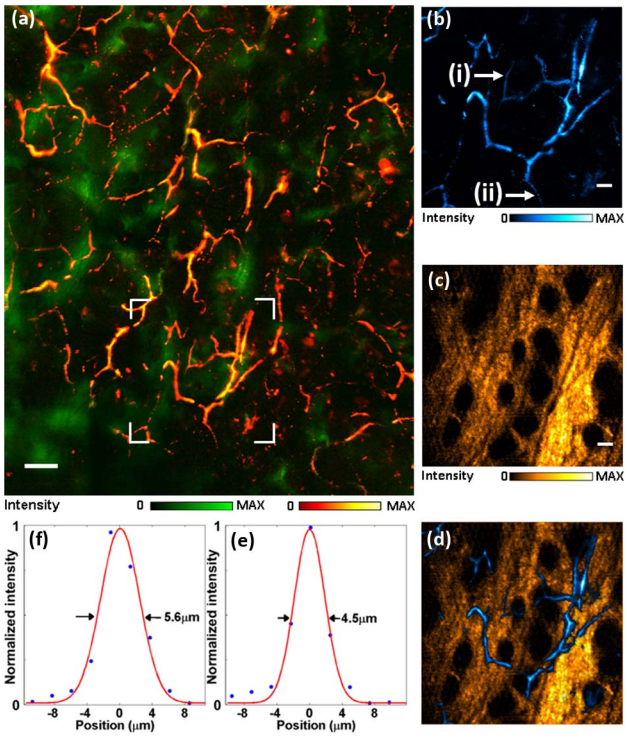

Fig. 4. Optoacoustic and second-harmonic generation imaging of the lower rear mouse abdomen *in vivo*. (a) Stitched optoacoustic microscopy image of a field of view measuring 1.8 mm × 2.2 mm, revealing a microvasculature network. Red corresponds to signals approximately 300 μm from the skin surface; green, to signals 200 μm deeper. Scale bar, 150 μm. (b) Higher-magnification view of the area bracketed in white (field of view, 630 μm × 630 μm) in (a). Acoustic signals of absorbers outside the image plane were removed by dividing the temporal signal. Scale bar, 50 μm. (c) Second-harmonic generation imaging of the area bracketed in white in (a), showing collagen structures. Scale bar, 50 μm. (d) Hybrid image of (b) and (c), indicating complementary contrast. (e, f) Gaussian fitting of the intensity in the cross-section of vessels (i) and (ii), indicated with arrows in (b), respectively.

displayed with magnification in Figs. 3(b) and 3(c), respectively. Intensity cross-sections [Figs. 3(d) and 3(e)] through the vessels indicated by arrows on Figs. 3(b) and 3(c) revealed vessel diameters as small as 6.4 μm (Gaussian fitting of raw data with $R^2 = 0.986$ and 0.948, respectively).

Next, we used our sensor to perform O2A intravital imaging of thick samples in epi-illumination mode. Optoacoustic images of areas of the abdomen of living mice [Fig. 4(a)] were obtained by stitching together an 1.8 mm × 2.2 mm area. Depth is shown color-coded: superficial signals originating from microvasculature branching into the dermis are shown by a "hot" color map and signals originating 200 μm deeper from bigger vasculature at the bottom of the dermis are shown by a green color map.

Superficial optoacoustic contrast was segmented [Fig. 4(b)] by plotting earlier temporal signals. The image shows the region of 630 μm × 630 μm boxed in Fig. 4(a), and depicts capillary networks entering and exiting the image plane in good detail. SHG images [Fig. 4(c)] were obtained over the same region as in Fig. 4(b). Bulges at the epidermis are visible in addition to well-defined collagen structures. The combination of early optoacoustic and SHG images [Fig. 4(d)] reveals co-localization of the complementary contrast. Cross-sectional intensities of individual vessels indicated by (i) and (ii) in Fig. 4(b) are displayed in Figs. 4(e) and 4(f), respectively. Analysis revealed vessel diameters as small as 4.5 and 5.6 μm (Gaussian fittings of raw data with $R^2 = 0.981$ and 0.974, respectively). SHG images obtained with a similar setup [30] (not shown) without the O2A sensor revealed a comparable quality. This confirms that the ultrasound gel inside the acoustic cavity of the new sensor does not interfere significantly with the optical modality.

3. DISCUSSION

We have demonstrated, for the first time to our knowledge, entirely optical intravital O2A microscopy in epi-illumination mode. The technique achieved *in vivo* imaging of thin tissue (mouse ear) and thick tissue (mouse abdominal dermis) enabled by a novel π-FBG-based sensor. This sensor is virtually invisible to

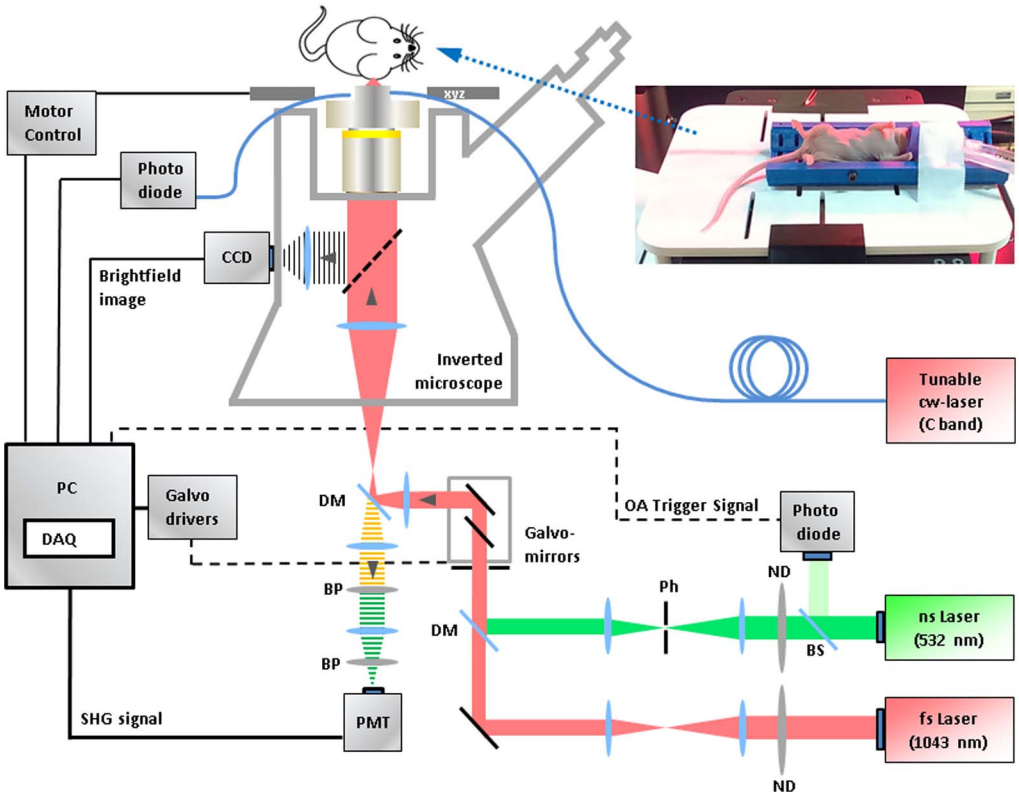

Fig. 5. Schematic depiction of the O2A microscopy setup: A standard inverted microscope with laser sources for optoacoustic and non-linear optical imaging is combined with galvanometric mirrors for fast laser raster scanning. The sensor is mounted on the microscope objective, with a tunable CW laser coupled to the embedded π-FBG. The inset shows the 3D printed platform supporting an anesthetized mouse and mounted on a *xyz* positioning stage. DM, dichroic mirror; BP, bandpass filter; PH, pinhole; ND, neutral density filter; BS, beam splitter; PMT, photomultiplier tube; OA, optoacoustic; DAQ, data acquisition card.

the optical path; therefore, it can be integrated with any optical microscope, allowing seamless O2A operation. This unique performance has been made possible by combining the ultra-miniaturized detector (125 μm diameter) with a bi-focal acoustic cavity, which projects the imaged plane inside the sample onto the detector. Moreover, by offering fivefold signal amplification, the cavity enables CW interrogation, which is significantly more cost-effective than previous demonstrations using CPRI. The new sensor covered an unprecedented aperture over ring resonators, which makes it better suited for imaging applications and potentially enables high scanning speeds.

The sensitivity of π-FBG varies directly with the Q factor of the optical cavity. Ultra-low linewidth interrogation and feedback mechanisms are typically required to lock the interrogating laser to the resonance of the optical cavity and impart high Q factors [27]. To meet these requirements, previous setups employed CRPI [14], which uses frequency comb pulses to interrogate the π-FBG resonance. However, CRPI requires expensive instrumentation and a complex actively stabilized output demodulator in order to maintain a high dynamic range. We demonstrated that a moderate-linewidth CW laser can provide interrogation of π-FBGs with moderate Q factor while leading to greater sensitivity than reported for CPRI. The NEP of our sensor (88 Pa) was lower than that of a sensor interrogated by CPRI (100 Pa), even though our Q factor was sixfold smaller (1.9×10^5 versus 1.14×10^6) [27]. The reduced sensitivity of the moderate Q factor was compensated by acoustic cavity signal amplification. Commercially available CW lasers should be easily tuned to the moderate Q factor π-FBG's resonance without locking mechanisms, exhibiting linear responses up to 0.75 MPa [31].

The optoacoustic integration in intravital setups can lead to next-generation optical microscopy, whereby multi-mode label-free detection of absorption contrast (optoacoustics) can be combined with optical readings to increase the information of the imaging session. Optoacoustic contrast reveals structural and functional variations in microvasculature associated with the diameters and density of blood vessels, and can enhance the information available to studies of hypertension, obesity, diabetes, inflammation, or angiogenesis [10,32,33]. This is particularly critical since optoacoustic detection is better suited than ultrasound for label-free imaging of microvasculature [34,35].

The sensitivity of the sensor presented can be further improved by embedding the Bragg grating onto thin-clad or polymer fibers with lower Young modulus [36,37], and by acoustically matching the fiber coating and medium inside the cavity.

Moreover, using microscope objectives with higher NA and longer working distances than in the sensor presented can result in improved resolution and imaging depth. In the future, a much richer optoacoustic visualization may be achieved by adding spectral capacity, resolving states of oxygenation, other tissue chromophores (melanin, myoglobin), externally administered optoacoustic agents, or optoacoustic reporter genes [38]. Seamless integration of optoacoustic detection in optical microscopy for intravital imaging opens up further possibilities for

generating a larger number of hybrid combinations based on fluorescence, confocal, multi-photon, and Raman microscopies.

4. MATERIALS AND METHODS

A. O2A System

The O2A microscope setup is illustrated schematically in Fig. 5. The two laser excitation beams were attenuated using a set of neutral density filters in order to adjust for different specimens, and then directed through a telescope and high-speed *xy*-galvanometric mirrors (6215H, Cambridge Technology, Bedford, MA, USA). In order to focus to a diffraction-limited spot, the combined beam was then enlarged to fill the back aperture of a 10*x* objective lens (PLN 10X, Olympus, Hamburg, Germany; NA 0.25, working distance (WD) 10.6 mm) that was mounted on an inverted microscope (AxioObserver.D1, Carl Zeiss, Jena, Germany). The beam was then raster-scanned across a 630 μm × 630 μm FOV during specimen imaging.

Specimens were aligned to the detector using a *xyz*-motorized microscopy stage (*xy*-stage, MLS203-2, Thorlabs, Newton, NJ, USA; *z*-stage, ZMZS500-E, Thorlabs; step size 0.1 μm). A 3D-printed platform was attached to the *xyz* stage using an inlay of thin polyethylene foil. This platform allowed the immobilization of samples ranging from micrometer-sized phantoms to living mice, together with the necessary anesthesia equipment. A drop of centrifuged ultrasound gel was placed between the platform and sensor to allow transmission of acoustic signals.

Second-harmonic generation microscopy was carried out using an Yb-based, 1043 nm laser (YBIX, Time-Bandwidth, Zürich, Switzerland) with a pulse width of 170 fs; average output power, 2.8 W; and repetition rate, 84.4 MHz. The nonlinear optical emission was collected through the objective lens in backward direction mode. The signal was split from the excitation wavelength using a dichroic mirror installed in an electrical filter wheel (CDFW5, Thorlabs). Then the signal was bandpass-filtered and recorded by a photomultiplier tube (PMT H9305-03, Hamamatsu Photonics, Hamamatsu, Japan).

Optoacoustic microscopy was performed using a 532 nm solid-state laser pumped by a pulsed diode (SPOT-10-100-532, Elforlight Ltd, Daventry, UK). The repetition rate was 0–50 kHz; energy per pulse, 20 μJ; pulse width, <1.4 ns; and $M < 1.1$. The laser pulses were detected using a photodiode (DET36A, Thorlabs), which triggered the galvanometric mirrors as well as signal acquisition. The ultrasound sensor was mounted on top of the microscope objective using an adapter plate [Fig. 1(a)].

B. Acoustic Cavity

The ellipsoidal shape of the acoustic cavity, made by CNC carving out of stainless steel, had a semi-major axis of 4.8 mm and a semi-minor axis of 4.1 mm. Its specific acoustic impedance was 47 Mrayl, 31-fold higher than that of water and nearly fourfold higher than that of glass [39]. The theoretical minimum and maximum reflection coefficients at the interface between the coupling medium and the cavity surface is 0.91 and 1 [40], corresponding to minimum and maximum incident angles of 0° and 31.3°. The high acoustic reflection coefficient and the malleability of stainless steel make this material well suited to serve as an acoustic mirror.

The dimensions of the cavity were chosen to both maximize the solid angle and minimize ultrasound attenuation. The maximum acoustic amplitude amplification (A) of the cavity can be estimated purely from the solid angles:

$$A = [(\Omega_{\mathbf{cav}} - \Omega_{\mathbf{exc}})/\Omega_{\mathbf{fib}})]^{1/2}. \quad (1)$$

Here, $\Omega_{\mathbf{cav}} = 5.59$ **sr**, $\Omega_{\mathbf{exc}} = 0.095$ **sr**, and $\Omega_{\mathbf{fib}} = 0.028$ **sr** correspond to the solid angles of the cavity, aperture for the excitation beam, and solid angle of the fiber sensor, respectively. Equation (1) yields an amplification of 14 and the difference to the recorded amplification results from attenuation of ultrasound due to the additional propagation length in the cavity [41], as well as from misalignments and the frequency response of the cavity. The latter is governed by surface imperfections due to limitations in manufacturing quality and the reflection coefficient of the solid/fluid interface affecting both phase and amplitude of the reflected wave as a function of the incidence angle. These imperfections interfere with the coherent summation of high-frequency waves, and the global effect resembles a low-pass filter.

The aperture at the bottom of the cavity was sealed using a standard circular microscope cover slip with a thickness of 170 μm. The cavity was filled with centrifuged ultrasound gel to allow for acoustic impedance matching; then it was sealed using 10 μm thick polyethylene foil. Most of this ellipsoidal cavity could be exploited because π-FBGs have a radial detection angle of 360° and an effective sensing length of 300 μm along the fiber axis [42].

C. π-FBG

Optoacoustic signals were detected using a π-FBG (TeraXion, Quebec City, Canada) which was embedded within the acoustic cavity of the sensor and which was interrogated using a tunable CW laser (INTUN TL1550-B, Thorlabs; 1520–1630 nm, 20 mW). Transmitted light was directed to a high-bandwidth photodiode (PDB450C, Thorlabs; detection bandwidth, 150 MHz), which detected changes in the transmitted intensity. This signal was recorded using a high-speed 12-bit data acquisition (DAQ) card (ADQ412, SP Devices, Linköping, Sweden), which allowed streaming-like acquisition and therefore high-speed raster scanning of the FOV. Analogous to Fabry–Perot interferometers [43], a π-FBG spectrum consists of a narrow resonance fringe in addition to a stop band centered on this fringe. We used a π-FBG with a resonance width of 8 pm at –3 dB and an overall grating length of 4 mm, similar to previous designs [31]. The π-FBG was UV-written into a standard single-mode polarization-maintaining fiber. The grating was created by periodically changing the refractive index along the fiber. An artificial defect resembling a gap (π-shift) between two distributed mirrors was added in the center of the grating. In this scheme, light is confined around this gap and spread over an effective length inversely proportional to the Q factor. The full width at half-maximum (FWHM) of the resonance is a measure of the Q factor and consequently of the sensitivity of ultrasound detection. Ultrasound-induced perturbations of the effective refractive index of the cavity arising from the elasto-optic effect were monitored. These perturbations shift the resonance in the transmission spectrum of the π-FBG, and thereby alter the intensity of light transmitted through the π-FBG.

D. Image Acquisition

The FOV (maximum, 630 μm × 630 μm) was raster-scanned by the laser excitation beams for optoacoustic and optical modalities using galvanometric mirrors controlled by a 16-bit DAQ card (PCIe 6363, National Instruments, Austin, Texas, USA) with a maximum sampling rate of 900 MS/s per channel. Resolution and step size were adjustable. After each scan, specimens were moved by the *xyz* stage to align the next area with the beams in order to allow stitching of larger images. The repetition rate of the optoacoustic microscopy excitation laser was 25 kHz, and the detected signals were bandpass-filtered (5–90 MHz).

E. Phantom Experiments

The sensor was characterized using two phantoms. The ability of the acoustic cavity to amplify the signal was examined using a custom-built pair of intercrossed sutures (Dafilon Polyamide, B. Braun Melsungen AG, Melsungen, Germany), each with a diameter of 19 μm. This cross was scanned laterally. Images in Figs. 2(c) and 2(d) were acquired at a resolution of 130 × 130 pixels and a pixel size of 4.84 μm. A total of 30 signals were averaged, corresponding to an acquisition time of 20 s. A typical SNR of the signal was 39.8 for 30 averages, corresponding to a SNR of 7.3 without averaging.

The lateral resolution of the sensor was measured by laterally scanning the edge of an SOI block (IMEC, Leuven, Belgium) that had a cross-sectional facet area of 0.8 mm × 3 mm and that was polished to optical grade to ensure a smooth edge [Fig. 2(e)]. The block was mounted with the polished facet facing the sensor. The area framed in white in Fig. 2(e) was acquired at a resolution of 50 × 50 pixels and a pixel size of 0.63 μm. Figure 2(f) shows the MIP in this area after averaging of 150 signals with an acquisition time of 15 s. Figure 2(g) shows the edge spread function along the dashed line in Fig. 2(f) as well as the line spread function. Based on the FWHM of the line spread function, we determined the lateral resolution of optoacoustic microscopy in our setup to be 3.7 μm.

F. *In vivo* Mouse Imaging

Animal experiments were approved by the government of Upper Bavaria. Optoacoustic and second-harmonic generation imaging was performed on female Nude-1 Foxn1 mice aged 10–12 weeks (Harlan Laboratories, Germany). Mice were anesthetized using 1.8% isoflurane and lain onto the imaging window of the 3D-printed platform mounted atop the *xyz* stage. Images were acquired with galvanometric mirrors scanning at a resolution of 170 × 170 pixels and pixel size of 2.4 μm. The laser repetition rate was 25 kHz and 100 signals were averaged, corresponding to an acquisition time of 116 s for a FOV of 170 × 170 pixels.

The mouse ear was imaged with the mouse lying on its side throughout the measurements. The mouse ear remained immobile because of the viscosity of a thin layer of centrifuged ultrasound gel between the ear and the sensor. A total of 36 images were acquired and stitched with an overlap of 60 μm in order to provide the image in Fig. 3(a).

The mouse rear abdomen was imaged with the animal lying on its back throughout the measurements. A thin layer of centrifuged ultrasound gel was applied onto the skin. A total of 30 images were acquired and stitched with an overlap of 42 μm to provide the image in Fig. 4(a).

During *in vivo* imaging and when scanning at minimal depths of around 50 μm, laser fluence did not exceed 15 mJ/cm^2. This is well below the ANSI limit of 20 mJ/cm^2 for maximal permitted visible-light laser fluence on the surface of human skin [44].

Funding. Deutsche Forschungsgemeinschaft (DFG) (RO 4268/4-1, CRC 1123 (Z1)).

Acknowledgment. The authors would like to thank Thomas Gerlach for his technical expertise and manufacture of the acoustic cavity.

†These authors contributed equally to this work.

REFERENCES

1. R. Y. Tsien, "The green fluorescent protein," Annu. Rev. Biochem. **67**, 509–544 (1998).
2. E. B. Brown, R. B. Campbell, Y. Tsuzuki, L. Xu, P. Carmeliet, D. Fukumura, and R. K. Jain, "In vivo measurement of gene expression, angiogenesis and physiological function in tumors using multiphoton laser scanning microscopy," Nat. Med. **7**, 864–868 (2001).
3. S. Hampel, P. Chung, C. E. McKellar, D. Hall, L. L. Looger, and J. H. Simpson, "Drosophila Brainbow: a recombinase-based fluorescence labeling technique to subdivide neural expression patterns," Nat. Methods **8**, 253–259 (2011).
4. M. Rudin and R. Weissleder, "Molecular imaging in drug discovery and development," Nat. Rev. Drug Discov. **2**, 123–131 (2003).
5. W. R. Zipfel, R. M. Williams, and W. W. Webb, "Nonlinear magic: multiphoton microscopy in the biosciences," Nat. Biotechnol. **21**, 1369–1377 (2003).
6. C. W. Freudiger, W. Min, B. G. Saar, S. Lu, G. R. Holtom, J. C. Tsai, J. X. Kang, and X. S. Xie, "Label-free biomedical imaging with high sensitivity by stimulated Raman scattering microscopy," Science **322**, 1857–1861 (2013).
7. J. Yao and L. V. Wang, "Photoacoustic microscopy," Laser Photon. Rev. **7**, 1–36 (2014).
8. G. J. Tserevelakis, D. Soliman, M. Omar, and V. Ntziachristos, "Hybrid multiphoton and optoacoustic microscope," Opt. Lett. **39**, 1819–1822 (2014).
9. B. Rao, F. Soto, D. Kerschensteiner, and L. V. Wang, "Integrated photoacoustic, confocal, and two-photon microscope," J. Biomed. Opt. **19**, 36002 (2014).
10. M. Omar, M. Schwarz, D. Soliman, P. Symvoulidis, and V. Ntziachristos, "Pushing the optical imaging limits of cancer with multi-frequency-band raster-scan optoacoustic mesoscopy (RSOM)," Neoplasia **17**, 208–214 (2015).
11. M. Seeger, A. Karlas, D. Soliman, J. Pelisek, and V. Ntziachristos, "Multimodal optoacoustic and multiphoton microscopy of human carotid atheroma," Photoacoustics **4**, 102–111 (2016).
12. E. M. Strohm, M. J. Moore, and M. C. Kolios, "Single cell photoacoustic microscopy: a review," IEEE J. Sel. Top. Quantum Electron. **22**, 6801215 (2016).
13. W. Song, Q. Xu, Y. Zhang, Y. Zhan, W. Zheng, and L. Song, "Fully integrated reflection-mode microscopy in vivo," Sci. Rep. **6**, 1–8 (2016).
14. A. Rosenthal, S. Kellnberger, D. Bozhko, A. Chekkoury, M. Omar, D. Razansky, and V. Ntziachristos, "Sensitive interferometric detection of ultrasound for minimally invasive clinical imaging applications," Laser Photon. Rev. **8**, 450–457 (2014).
15. J. Yao and L. V. Wang, "Sensitivity of photoacoustic microscopy," Photoacoustics **2**, 87–101 (2014).
16. W. Song, W. Zheng, R. Liu, R. Lin, H. Huang, X. Gong, S. Yang, R. Zhang, and L. Song, "Reflection-mode in vivo photoacoustic microscopy with subwavelength lateral resolution," Biomed. Opt. Express **5**, 4235–4241 (2014).
17. S. Hu, K. Maslov, and L. V. Wang, "In vivo functional chronic imaging of a small animal model using optical-resolution photoacoustic microscopy," Med. Phys. **36**, 2320–2323 (2009).
18. J. Yao, L. Wang, J.-M. Yang, K. I. Maslov, T. T. W. Wong, L. Li, C.-H. Huang, J. Zou, and L. V. Wang, "High-speed label-free functional

photoacoustic microscopy of mouse brain in action," Nat. Methods **12**, 407–410 (2015).
19. K. Sathiyamoorthy, E. M. Strohm, and M. C. Kolios, "Low-power noncontact photoacoustic microscope for bioimaging applications," J. Biomed. Opt. **22**, 46001 (2017).
20. P. Hajireza, W. Shi, K. Bell, R. J. Paproski, and R. J. Zemp, "Non-interferometric photoacoustic remote sensing microscopy," Light Sci. Appl. **6**, e16278 (2017).
21. X. Zhu, Z. Huang, G. Wang, W. Li, D. Zou, and C. Li, "Ultrasonic detection based on polarization-dependent optical reflection," Opt. Lett. **42**, 439–441 (2017).
22. S.-L. Chen, L. J. Guo, and X. Wang, "All-optical photoacoustic microscopy," Photoacoustics **3**, 143–150 (2015).
23. Z. Xie, S.-L. Chen, T. Ling, L. J. Guo, P. L. Carson, and X. Wang, "Pure optical photoacoustic microscopy," Opt. Express **19**, 9027–9034 (2011).
24. H. Li, B. Dong, Z. Zhang, H. F. Zhang, and C. Sun, "A transparent broadband ultrasonic detector based on an optical micro-ring resonator for photoacoustic microscopy," Sci. Rep. **4**, 4496 (2014).
25. B. Dong, L. Hao, Z. Zhang, K. Zhang, S. Chen, C. Sun, and H. F. Zhang, "Isometric multimodal photoacoustic microscopy based on optically transparent micro-ring ultrasonic detection," Optica **2**, 169–176 (2015).
26. G. Wissmeyer, D. Soliman, R. Shnaiderman, A. Rosenthal, and V. Ntziachristos, "All-optical optoacoustic microscope based on wideband pulse interferometry," Opt. Lett. **41**, 1953–1956 (2016).
27. A. Rosenthal, D. Razansky, and V. Ntziachristos, "Wideband optical sensing using pulse interferometry," Opt. Express **20**, 19016–19029 (2012).
28. R. K. Jain, L. L. Munn, and D. Fukumura, "Dissecting tumour pathophysiology using intravital microscopy," Nat. Rev. Cancer **2**, 266–276 (2002).
29. M. Choi, S. J. J. Kwok, and S. H. Yun, "In Vivo fluorescence microscopy: lessons from observing cell behavior in their native environment," Physiology **30**, 40–49 (2015).
30. D. Soliman, G. J. Tserevelakis, M. Omar, and V. Ntziachristos, "Combining microscopy with mesoscopy using optical and optoacoustic label-free modes," Sci. Rep. **5**, 12902 (2015).
31. A. Rosenthal, D. Razansky, and V. Ntziachristos, "High-sensitivity compact ultrasonic detector based on a pi-phase-shifted fiber Bragg grating," Opt. Lett. **36**, 1833–1835 (2011).
32. M. Brissova, A. Shostak, C. L. Fligner, F. L. Revetta, M. K. Washington, A. C. Powers, and R. L. Hull, "Human islets have fewer blood vessels than mouse islets and the density of islet vascular structures is increased in Type 2 diabetes," J. Histochem. Cytochem. **63**, 637–645 (2015).
33. C. L. Y. Zhao, Y.-P. Zheng, and G. L. Y. Cheing, "The association between skin blood flow and edema on epidermal thickness in the diabetic foot," Diabetes Technol. Ther. **14**, 602–609 (2012).
34. A. Taruttis and P. C. Wouters, "Optoacoustic imaging of human vasculature: feasibility by using a handheld probe," Radiology **281**, 256–263 (2016).
35. S. Laurent and P. Boutouyrie, "Large and small artery alterations," Circ. Res. **116**, 1007–1021 (2015).
36. I. A. Veres, P. Burgholzer, T. Berer, A. Rosenthal, G. Wissmeyer, and V. Ntziachristos, "Characterization of the spatio-temporal response of optical fiber sensors to incident spherical waves," J. Acoust. Soc. Am. **135**, 1853–1862 (2014).
37. H. Grün, T. Berer, K. Pühringer, R. Nuster, G. Paltauf, and P. Burgholzer, "Polymer fiber detectors for photoacoustic imaging," Proc. SPIE **7564**, 75640M (2010).
38. J. Stritzker, L. Kirscher, M. Scadeng, N. C. Deliolanis, S. Morscher, P. Symvoulidis, K. Schaefer, Q. Zhang, L. Buckel, M. Hess, U. Donat, W. G. Bradley, V. Ntziachristos, and A. A. Szalay, "Vaccinia virus-mediated melanin production allows MR and optoacoustic deep tissue imaging and laser-induced thermotherapy of cancer," Proc. Natl. Acad. Sci. U.S.A. **110**, 3316–3320 (2013).
39. T. Kundu, *Ultrasonic Nondestructive Evaluation* (CRC Press, 2004).
40. R. G. Maev, *Acoustic Microscopy: Fundamentals and Applications* (Wiley-VCH, 2008).
41. J. D. N. Cheeke, *Fundamentals and Applications of Ultrasonic Waves* (CRC Press, 2002).
42. A. Rosenthal, M. Á. A. Caballero, S. Kellnberger, D. Razansky, and V. Ntziachristos, "Spatial characterization of the response of a silica optical fiber to wideband ultrasound," Opt. Lett. **37**, 3174–3176 (2012).
43. T. Fink, Q. Zhang, W. Ahrens, and M. Han, "Study of π-phase-shifted, fiber Bragg gratings for ultrasonic detection," Proc. SPIE **8370**, 1–7 (2012).
44. L. V. Wang, *Photoacoustic Imaging and Spectroscopy* (CRC Press, 2009).